Nexo Revista Científica
Vol. 36, No. 03, pp. 422-438/Junio 2023

ISSN-E 1995-9516
Universidad Nacional de Ingeniería

http://revistas.uni.edu.ni/index.php/Nexo
https://doi.org/10.5377/nexo.v36i03.16464

Using the band ratio approach, FULL-PIXEL (SAM and SFF) and SUB-PIXEL (MF and SID) methodologies to discover areas with alteration using the Aster sensor: a case study in north westen Iran - Sivardaghi Area

Uso del enfoque de relación de banda, metodologías FULL-PIXEL (SAM y SFF) y SUB-PIXEL (MF y SID) para descubrir áreas con alteración usando el sensor Aster: un estudio de caso en el noroeste de Irán - Área de Sivardaghi

Majid Bagheri[1], Afshin Ashja Ardalan[2]*, Alireza Ganji[3], Saeed Hakimi Asiabar[3], Mohammad Ali Arin[2]

[1]Faculty of Science, North Tehran Branch, Islamic Azad University, Tehran, Iran
[2]Department of Geology, North Tehran Branch, Islamic Azad University, Tehran, Iran
[3]Department of Geology, Lahijan Branch, Islamic Azad University, Lahijan, Iran

*email: afshinashjaardalan@yahoo.com

(recibido/received: 05-febrero-2023; aceptado/accepted: 08-mayo-2023)

ABSTRACT

ASTER sensor data is among the most potent satellite data accessible for doing geological investigations, with images for the whole earth's surface. In order to test the capability of this sensor to detect places with geochemical alterations, photographs of Mount Seiver Daghi in the western Iranian province of Samal were utilized in this study. This region, which comprises of magmatic and volcanic terrain, is part of the Arsbaran territory and is covered by intrusive masses with alluvial and sedimentary deposits. To conduct this study, an ASTER measuring frame was utilized, which, after performing atmospheric corrections using the internal average relative reflectance (IARR) method of false color composite images and principal component analysis (PCA), was able to differentiate between different lithological units using the Band assignment method, full-pixel methods of spectral angle mapper (SAM) and base spectrum algorithm of spectral feature fitting (SFF) as well as sub-pixel methods of matched filtering. The study demonstrates that the approach of principal component analysis and false color composition is efficient for distinguishing sedimentary rock units from igneous rock units, and its application is suggested for the designated rock units. Due to the lack of spectral characteristics of feldspars and quartz in the short infrared wavelength range, the basic spectrum methods utilized in this work are incapable of identifying such minerals. It is not advised to use these algorithms to distinguish between various magmatic units.

Keywords: Geochemical alteration detection, full-pixel and sub-pixel mapping, spectral angle mapper method, matching filter algorithm and pure endmember

RESUMEN

Los datos del sensor ASTER se encuentran entre los datos satelitales más potentes accesibles para realizar investigaciones geológicas, con imágenes de toda la superficie de la tierra. Para probar la capacidad de este sensor para detectar lugares con alteraciones geoquímicas, en este estudio se utilizaron fotografías del monte

Seiver Daghi en la provincia iraní occidental de Samal. Esta región, que comprende terreno magmático y volcánico, es parte del territorio de Arsbaran y está cubierta por masas intrusivas con depósitos aluviales y sedimentarios. Para realizar este estudio se utilizó un marco de medición ASTER, el cual, luego de realizar correcciones atmosféricas mediante el método de reflectancia relativa promedio interna (IARR) de imágenes compuestas de falso color y análisis de componentes principales (PCA), fue capaz de diferenciar entre diferentes unidades litológicas utilizando el método de asignación de banda, los métodos de píxel completo del mapeador de ángulo espectral (SAM) y el algoritmo de espectro base de ajuste de características espectrales (SFF), así como los métodos de subpíxel de filtrado adaptado. El estudio demuestra que el enfoque del análisis de componentes principales y la composición de colores falsos es eficiente para distinguir las unidades de roca sedimentaria de las unidades de roca ígnea, y se sugiere su aplicación para las unidades de roca designadas. Debido a la falta de características espectrales de los feldespatos y el cuarzo en el rango de longitud de onda del infrarrojo corto, los métodos de espectro básicos utilizados en este trabajo son incapaces de identificar dichos minerales. No se recomienda utilizar estos algoritmos para distinguir entre varias unidades magmáticas.

Palabras clave: Detección de alteraciones geoquímicas, mapeo de píxeles completos y subpíxeles, método de mapeo de ángulo espectral, algoritmo de filtro coincidente y miembro final puro

1. INTRODUCTION

The ASTER sensor is one of the instruments installed on the 2000-launched Tera satellite, which captures multispectral data in 14 bands. This sensor has 5 bands in the mid-infrared area of the electromagnetic spectrum (8-14 m) and 9 bands in the SWIR range (1.4-2.5 m), which are mostly used to detect carbonate and clay minerals (Rockwell and Hofstra 2008). The Anjard region, which is part of Iran's Arsbaran zone, consists primarily of volcanic and magmatic rocks that have merged with sedimentary rocks. Due to the boiling of the region's magmatic effluents, mineralization has occurred in some locations. Since the spectrum properties of minerals in igneous rocks are similar to one another, ASTER gauge data have not been frequently employed for mapping igneous terrains. In this study, an attempt was made to map the examined area utilizing a combination of techniques, including the pixel purity index, spectral angle mapper, and band ratios.

2. GEOLOGY

The researched area is located 25 to 70 kilometers northwest of Ahar city in the province of East Azerbaijan. The examined area encompasses around 170 square kilometers and includes a portion of the Arsbaran region and the Alborz magmatic zone with undulating topography (Alavi, 2018; Yazdi et al. 2022). Granites, monzogranites, and other igneous and volcanic rocks cover around fifty percent of the region. Multiple periods of igneous and volcanic activity led to the production of many intrusions, volcanic rocks, and tuffs in the region from the Late Eocene to Oligocene (Agard et al. 2011). In this region, magmatism has caused contact metamorphism, metasomatism, and the creation of copper porphyry deposits and metamorphic rocks like hornfels (Bazin and Habner, 1969).

The sedimentary rocks of the study region are predominantly Cretaceous in age, with greater concentrations in the north and south. With a height of 2,640 meters, the highest mountain of the examined region corresponds to the Shiver Daghi intrusive mass, which intruded the Cretaceous sedimentary and volcanic rocks. In contact with the intrusive mass are observed skarn masses, silicification, recrystallization, and hornfels (Malai, 1993; Yazdi et al. 2019). In the southern portion of the region, the terrain is quite flat and there are significant Neogene alluvial sediments (Kansaran, 2018; Yazdi et al. 2016). Following is a concise explanation of the lithology of the rock units in the research region.

Cretaceous sedimentary rocks are more prevalent in the northern and southern portions of the study region. With a height of 2,640 meters, the tallest mountain of the examined region belongs to the Sivar Daghi intrusive mass, which has penetrated the volcanic rocks and Cretaceous deposits. In contact with the intrusion, masses of skarn, silicification, recrystallization, and hornfelses are detected (Malai, 1993; Naeemi et al. 2022). In the southern portion of the region, the terrain is generally flat and rich in Neogene sedimentary and alluvial deposits (Kansaran, 1368; Bazoobandi et al. 2015; Gharib-Gorgani et al. 2017; Bina et al. 2020). Following is a concise explanation of the lithology of the rock units in the research region.

The observable rock units in the research region consist of sedimentary rocks, volcanic rocks, volcanic debris, and igneous and volcanic rocks. On the geological map of the region, sedimentary rocks are designated with symbols such as Kl1, Kl,sh, Ksh, and Ks,sh based on the ratio of sedimentary to volcanic components. Kst, Kv, Kt,sh, Eag, and Plla (volcanic clastic rocks) and Ktc, Kan, Kta, Kda, Kvr, Emp, Qtb, Qan, and Qb (volcanic clastic rocks) (volcanic rocks).

Kl1 is constituted primarily of limestone, whereas Kl,sh, Ksh, Ks, and Ks,sh are made up of shale, sandstone, and trace amounts of limestone. Minor metamorphism has largely changed the Ksh sedimentary block into hornfelses and silicified schists. Many sedimentary rock units contain a large quantity of volcanic material and tuff in addition to pure rock. In addition to limestone and sandstone, conglomerates and river consolidation deposits such as Ksh,t, PlQc, Qt1 and PlQc include considerable amounts of volcanic elements and andositic tuffs. The riverbeds of Qt2, Qf, Qsc, Qdf, Qds, and Qc and Qal consist of older volcanic rocks. In the examined area, age distinctions across lithological units are uncommon. Nonetheless, a quick overview of the lithological units follows.

Ksh,t is composed of shale, agglomerate, tuff, and intermediate volcanic rocks such as andesite and dacite. In the Ksh,t unit, contact metamorphism caused by the incursion of Shiver Daghi has resulted to the creation of hornfels. Ktc consists of trachyandesite and latite that has undergone epidoteization.

Kan consists of basalt and andesite basalt in which the plagioclase minerals have been replaced by clay minerals, chlorite, carbonate minerals, and iron oxides.

Dacite, trachyandesite, latite, and andesite make up Kda and Ev. Kvr is composed of rhyolite, dacite, and acidic tuff, together with feldspars and ferromagnesian minerals that have been transformed into cercite and iron oxide. Qtb Qan and Qb consist of black basalt and trachy basalt with plagioclase and pyroxene phenocrysts. Emp is formed of latite that has been severely sericiticized. Kst, Kv, Kt, and sh are made of a mixture of tuff, shale, and sandstone. Eag consists of andesitic volcanic rocks and agglomerates that have been significantly changed. Plla is a lahar deposit composed of andesite and dacite with shards of siliceous rock.

The area has quartz monzonite and quartz-monzodiorite intrusive Shir Daghi masses (qmz-mzd). The intrusive mass demonstrates that ferromagnesium minerals and heterogeneity can be separated geographically. This intrusive material is oxidizing and contains magnetite formed by magma. Amphibole and biotite are ferromagnesium minerals. As a result of alteration, there are traces of epidote, chlorite, and sericite. At the contact point of the intrusive mass and primarily limestone units at the northernmost contact point with the intrusive mass, a tiny copper deposit forms (Anjard copper deposit). This region also contains quartz monzonite (d-qmd), granite (g), granodiorite (md-gb), and sinogabbro (sn-gb) (Moorhouse, 1985, Spear, 1993; Moghadam et al. 2021).

At the contact point with the Shir Daghi intrusive unit, Hornfels rock units (hp) consist of biotite, andalusite, cordierite, feldspar, and sillimanite (Mojran Alban Abad, 1382; Moinevaziri and Azizi 2023; Jalali Nezhad et al. 2023). Typically, metamorphism occurs at the mass-contact point in metabasites. In calc-silicate rocks,

epidote, tremolite, alkali feldspar, phlogopite garnet, and clinopyroxene are more prevalent (Mojran Alban Abad, 2012; Safari et al. 2022; Pirmohammadi Alishah 2023; Ashrafi et al. 2023). Skarn (sk) (sk) It is composed of garnet, pyroxene, actinolite, scapolite, and epidote, with minor sulfide and oxide minerals and highly abundant carbonate minerals at the point of contact with the Shir Daghi intrusive unit (Hoseinzadeh, 2018; Seyyedi et al. 2022; Rahimzadeh et al. 2022). The composition of the hal rock unit is epidote, albite, actinolite, and calcite. It contains quartz, chlorite, and garnet. This unit of rock is black in hue. In the form of plagioclase transformed into clay minerals and amphibole, one may observe the remnants of the principal minerals. In the form of malachite, there are traces of copper mineralization. Lithographic map Figure 1 depicts the simplified research region.

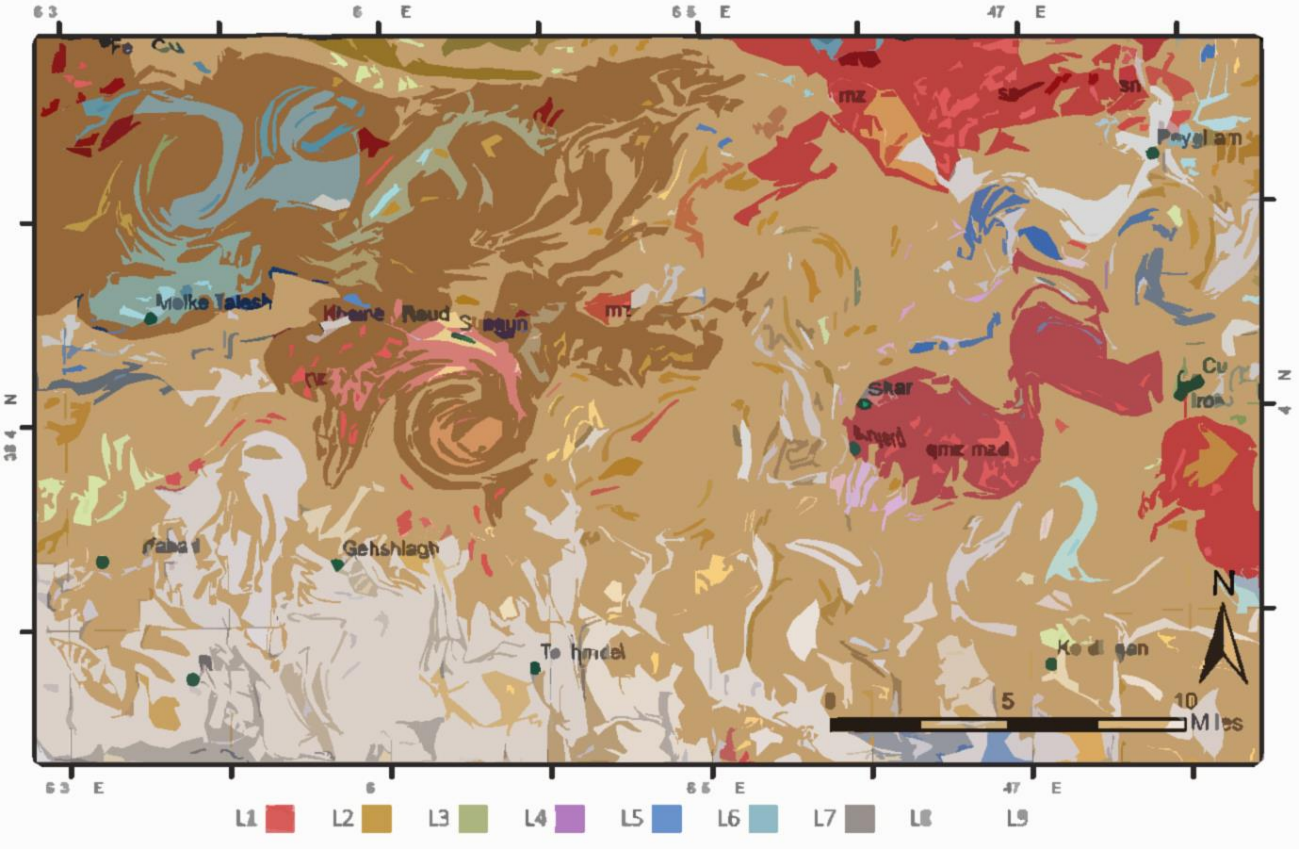

Fig. 1. A lithological map of the area under examination. L1: igneous and magmatic intrusive rocks, L2: volcanic rocks, L3: tuff and volcanoclastics, L4: shale, L5: sandstones, L6: limestone, L7: metamorphic rocks, L8: conglomerate, L9: alluvium

3. CORRECTIONS OF THE ATMOSPHERE AND IMAGE PROCESSING

Three VNIR spectral bands and six SWIR spectral bands of the ASTER sensor are superimposed for image processing, resulting in a spatial resolution of 15 meters for bands 1 through 3 of the ASTER sensor.
Before inputting satellite photos into spectral identification methods, atmospheric influences are frequently adjusted (Bernstein et al. 2012; Richter and Schlapfer 2013). Cruz's internal average relative reflectance (IARR) approach was used to adjust the image for atmospheric conditions (1988). IARR is a method (Kruse, 1988) that does not require data on atmospheric conditions and instead uses image band data. The IARR method can be utilized in locations with little vegetation cover and in the absence of atmospheric data necessary for accurate atmospheric correction via radiative transfer algorithms (RSI 2004; Gao et al. 2009).

Several studies of arid and semiarid environments have previously employed this technique with success (Kruse 1988; Ben-Dor and Kruse 1994; Rasouli Beirami and Tangestani 2020). In the IARR calibration, each pixel's brightness is normalized by the spectral band's mean radiance (Kruse 1988). The reflectance values obtained by IARR are relative reflectance and cannot be compared directly to the laboratory spectra of the materials. However, the IARR method's image reveals the form of the absorption features (Kruse 1988). PCA operates by computing the correlation coefficient between pixels and rearranging the original space vectors so that they coincide with the direction of greatest data alteration.

4. PRINCIPAL COMPONENT ANALYSIS

Principal component analysis (PCA) is a statistical technique for reducing the dimensionality of remote sensing data by translating it into a new orthogonal space (Yamaguchi and Naito 2003; Rajendran et al. 2011; Asadzadeh and de Souza Filho 2016). Consequently, the most significant changes in the spectral features of the picture pixels are readily apparent in PCA images. PCA operates by determining the correlation coefficient between pixels and rotating the principal space vectors to coincide with the direction of greatest data variance (Crosta and McMoore 1989). False color composites of PCA bands are frequently employed to differentiate between lithologies (Tangestani et al. 2008; Rajendran et al. 2011).

Purification of spectrum Due to the existence of a variety of materials with distinct spectra, minerals with varying grain sizes, and residual air absorption characteristics, the spectral shapes of the ASTER spectrometer image change from the laboratory spectrum. Even when converted to the standard bands of the ASTER analyzer, laboratory spectra cannot be used as a standard for picture categorization and detection of target chemicals. Therefore, in order to improve the performance of mapping algorithms, it is essential to select the image's cleanest spectrum (Boardman, et al. 1995). Pixel Purity Index (PPI) is one of the most efficient ways for getting pure spectra from an image (Boardman, et al. 1995). The pixel purity index algorithm translates pixel spectra onto a space-selected random vector and then counts the number of times each pixel appears at the end of the random vector. The pixels with the highest frequency of appearance at the end of the random vectors are chosen to have the clearest spectrum. To lessen the impact of noise on pixel representation, the pixel purity index approach employs normalized (MNF) noise pictures (Rowan and Mars 2003; RSI 2004). MNF images are comparable to PCA images with the exception that the image is changed by choosing the principal space vectors with the highest signal-to-noise ratio (Rajendran et al. 2013).

5. BAND RATIOS AND IMAGE HIGHLIGHTS

Band ratios of ASTER spectrometer pictures have been utilized successfully and extensively to describe spectral composition alterations by reducing albedo effects caused by changes in terrain slope, illumination circumstances, and grain size (Rowan and Mars 2003; Rowan, Mars, and Simpson 2005). Band ratios are so sensitive to spectral alterations that they may discriminate between dolomite and calcite (Rasouli Beirami and Tangestani 2020). Due to the fact that band ratios are insensitive to optical conditions, they can be utilized without difficulty for lithology mapping in an IAR-calibrated image (Kruse 1988; Rowan, Mars, and Simpson 2005). (Crowley et al. 1989; Crowley, 1993; Rowan, Mars, and Simpson, 2005; Rasouli Beirami and Tangestani, 2020)

6. SPECTRAL ANGLE MAPPING DEVICE

The Spectral Angle Mapper (SAM) technique gives a measure of similarity between a reference spectrum and an unknown spectrum by calculating the angle between two spectra under the assumption that both are vector values in an n-dimensional space (Kruse et al. 1993). The output of the SAM algorithm is an image displaying the spectral angle between the reference spectrum and the picture's pixel spectrum. Pixels with smaller divergence angles, or darker pixels, correlate to a greater number of reference spectra. Due to the

fact that the SAM algorithm is insensitive to image lighting conditions (Kruse et al., 1993), it can be applied to IAR images.

7. COMPLIANCE WITH SPECTRAL IMAGING STANDARDS (SFF)

The algorithm for spectral image matching uses the least squares method to compare image spectra with reference spectra. This approach adapts the pixel and target spectra by analyzing particular absorption patterns in the spectra. In this procedure, the continuum is first eliminated from the image and reference spectra, and then the image spectrum is compared to the reference spectrum using the deep least squares methodology and the shape of the spectral pictures. The outputs of each reference spectrum are represented by a scale image and either a root mean square error image or an adaptation image in this algorithm. Brighter pixels in the scale image indicate a closer match to the reference material. The black pixels in the root mean square error image indicate a reduced mistake, and when combined with the results of the scale image, they can be used to locate the areas that match the reference spectrum using a two-dimensional scatter diagram.

8. COMPATIBLE FILTERING

Matched filtering (MF) is a spectral separation technique that identifies the endmembers of defined abundance spectra by employing a partial separation technique. Boardman, Cruz, and Green were the originators of the MF technique (1995). The primary advantage of the MF approach is that it is not necessary to know all the image's end members. The MF technique maximizes the endmember reaction while removing the background effect. The probability of a match between a pixel's spectrum and the spectrum of the target material increases as the output of the MF technique for that pixel increases.

9. DIVERGENCE OF SPECTRA INFORMATION (SID)

The spectral information divergence classification method is a spectral classification approach that use the size of the divergence to match pixels to the relevant spectrum. In this strategy, the pixels are more likely to be comparable the lesser the divergence. Also, pixels over the maximum threshold for divergence are not categorized.

10. DISCUSSION

10-1. mineral spectral characteristic

Feldspars

Due to doubly positive iron oxides, the visible and near-infrared (0.35–2.50 m) spectral characteristics of feldspars are characterized by diffuse absorption features in the wavelength range of approximately 1.1–1.3 m. If water is incorporated into its structure, there may also be water absorption. The absorption wavelength becomes twice as positive as the iron level increases. The absorption bands that correspond to the highest level of doubly positive iron (over 0.5wt%) are the deepest. Fe content increases twofold as anorthite content increases up to An65. Plagioclase shows no spectral characteristics in the 2.1–2.5 m wavelength range, with the exception of diffuse absorption in the 1.1–1.3 m wavelength region. Reflectance is relatively strong at visible spectrum wavelengths. The band ratio (b2+b3)/(b7+b8) can be utilized to calculate the ratio of plagioclase to ferromagnesium minerals (Adams and Goullud 1978; Crown and Pieters 1987).

Olivine, epidote, chlorite, and pyroxene

Both ferric iron (double positive) and iron in minerals induce considerable absorption between 0.8 and 2.4 micrometers in wavelength. Frequently, ferric minerals exhibit absorption about 0.9 m. (Hunt 1977; Horgan

et al. 2014). Iron's strongest absorption band ranges between 0.9 and 1.4 m, typically between 1.0 and 1.1 m. Numerous iron-containing minerals, such as pyroxenes, also exhibit a second absorption band, which is typically near 2 m, but can range between 1.8 and 2.4 m. The absorption bands of orthopyroxene are relatively narrow about 0.9 m and rather large around 1.9 m. Clinopyroxenes with high and low calcium behave differently. Certain clinopyroxenes exhibit a narrow, symmetrical absorption band centered around 1.05 m and a large absorption band centered about 2.20 m. Other kinds of clinopyroxene may exhibit a complicated absorption band about 1.0 m as opposed to 2.0 m. (Horgan et al., 2014) The 1.0 m band is actually composed of two or three distinct bands centered at 0.94, 1.03, and 1.15 m. (Figure 2).

Olivine has a large, asymmetric absorption band centered at 1.05 m, but none at 2.0 m. The 1.0 m band consists of three bands with centers near 0.85, 1.05, and 1.15 m. (Horgan et al. 2014). Other iron-bearing minerals, including iron oxides, iron-bearing clay minerals, and iron sulfates, typically exhibit absorption bands between 0.9 and 1.1 m. (Horgan et al. 2014). Strong absorption of ferric iron (Fe+3) occurs at a wavelength of around 0.45 micrometers, which corresponds to the band of an ASTER detector. Epidote, chlorite, and other ferromagnesium minerals containing hydroxyl groups exhibit high absorption for F-OH vibrations between 2.20 and 2.30 micrometers in wavelength, which corresponds to bands 8 and 7 of the ASTER meter (Clark et al. 1990).

Quartz

Quartz lacks unique absorption characteristics in the SWIR spectral band. Consequently, multispectral thermal infrared (TIR) data from ASTER spectrometers are indispensable for detecting non-hydrous forms of quartz (Rockwell and Hofstra 2008). This corresponds to band 11 of the ASTER gauge, which permits mapping of acidic and igneous volcanic rocks (Rockwell and Hofstra, 2008; Rajendran et al., 2011). The spatial resolution of the ASTER meter's thermal infrared data is 90 meters, therefore thermal bands cannot be used to successfully identify siliceous rocks (Rasouli Beirami and Tangestani 2020). Due to hydroxyl vibrations, a variety of hydrous quartz in silicate minerals may exhibit absorption in band 4 of the ASTER gauge (Rajendran and Nasir 2014).

Carbonate minerals

Carbonate rocks consist primarily of calcite and dolomite. Dolomite and calcite possess distinctive spectral properties ((Hunt et al. 1972; Hunt 1977; Rasouli Beirami and Tangestani 2020)). The absorption band of calcite at 2.35 m corresponds to band 8 on the ASTER meter, whereas the absorption band of dolomite at 2.33 m corresponds to band 7 (Zaini et al. 2014)). Calcite and dolomite can be separated and recognized based on the difference in wavelength absorption between 2.33 and 2.45 m. (Rowan and Mars 2003). In the thermal infrared range, calcite and dolomite exhibit considerable absorption at wavelengths of 11.40 and 11.35 micrometers, respectively (Rockwell and Hofstra 2008). (Rajendran et al. 2011). Dolomite and calcite can be recognized using the ASTER meter band ratio b8/b7 (Rasouli Beirami and Tangestani, 2020). (Figure 2).

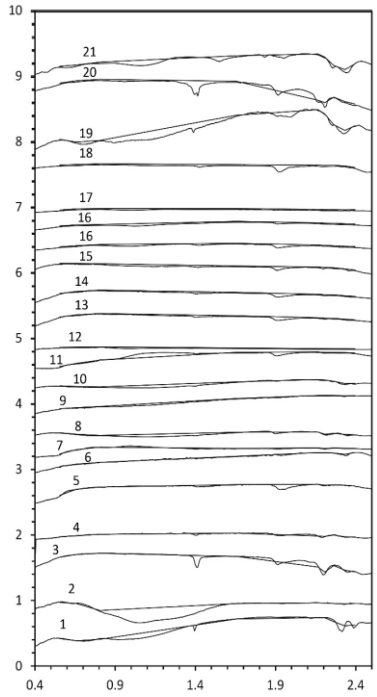

Fig. 2. The spectrum of rich minerals and rocks in igneous and sedimentary environments is depicted in Figure 2. 1. amphibole, 2. olivine, 3. illite, 4. quartzite, 5. feldspar, 6. limestone, 7. sandstone, 8. illite shale, 9. granodiorite, 10. diorite, 11. rhyolite, 12. basalt Andesite, 13. Quartz monzonite, 14. Quartz monzonite, Nepheline syenite and Nepheline, 16. Weathered basalt, 17. Pyroxene basalt, 18. Fresh basalt, 19. 20. Chlorite, 21. Kaolinite, 22. Epidote

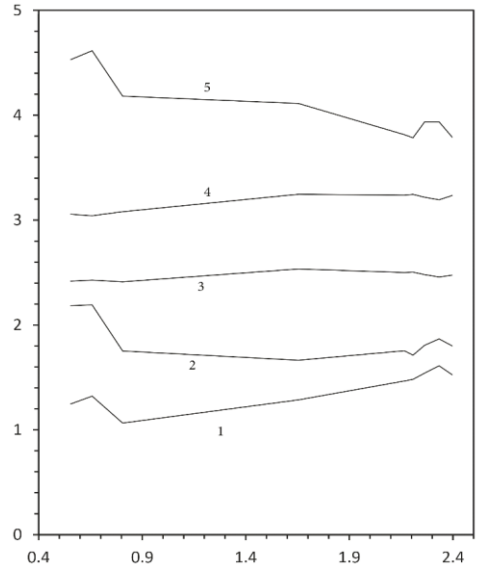

Fig. 3. Spectra derived from IAR image, 1: dark igneous/volcanic rocks with increased pyroxene content, 2 and 3: sediments, 4: igneous/volcanic rocks, 5: severely changed rocks with ferric iron absorption.

Clay sediments

Clay minerals, including kaolinite and mica, exhibit Al-OH absorption characteristics near wavelengths of 2.10 to 2.20 m. Additionally, the hydroxyl group shows a twofold absorption at approximately 1,4 m. Illite and muscovite contain extra absorption bands between 2.35 and 2.40 microns. Mg-OH absorbs light at a wavelength of approximately 2.30 microns (Clark et al. 1990). Therefore, these hydroxyl absorption characteristics can be recognized using the ASTER probe's band 6 (Figure 2).

10-2. PCA image (principal component analysis)

Since vegetation is regarded as a destructive spectral element in PCA transformation (Grebby et al., 2014), the vegetated and cultivated parts of the image were masked with an NDVI mask. Figure 4 depicts the composite fake color image formed by assigning PCA b1,b2,b3 to RGB. The majority of sedimentary and alluvial rocks are depicted in green, while the majority of igneous and volcanic rocks are depicted in red. Numerous regions covered by black basalts (Qp) are depicted in red. There are, however, a few exceptions. Red indicates sedimentary units such as shale, represented by Ksh,t. Some volcanic and igneous rocks, marked by r01, r02, and r03, are depicted in green. The findings of PCA indicate that the spectral differences between the various rock units in the region are somewhat minor. Aside from that, the PCA image reveals glaring disparities between several lithological units. PCA imaging is frequently utilized to reveal these distinctions ((Rajendran et al., 2011)).

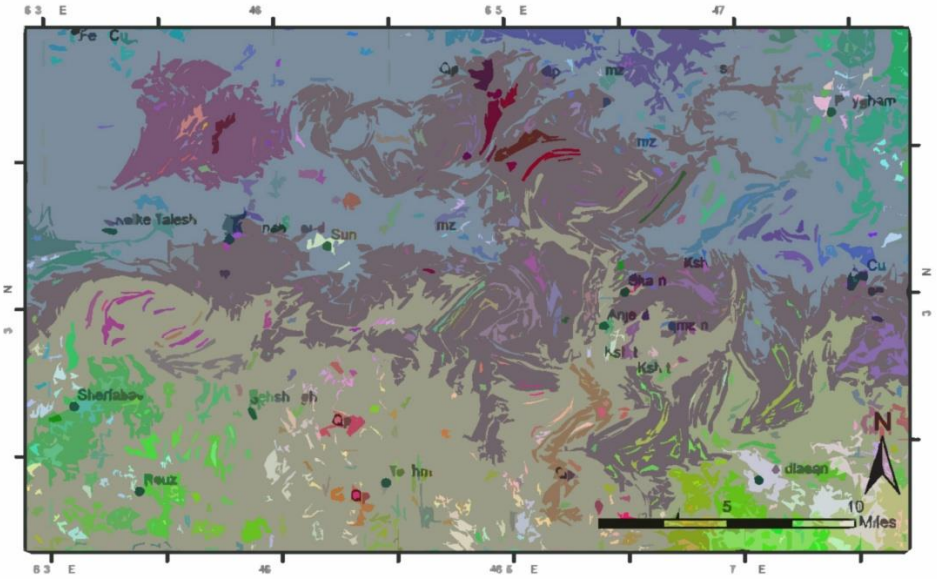

Fig. 4. depicts the creation of a false color composition from a PCA picture by assigning PC1, PC2, and PC3 to an RGB color image. High PC1 levels cause dark basalts and pyroxene basalts to appear mostly red. Monzonites (mz) and hot milk quartz monzonite (qmz-mzd) are red or crimson-blue in color. Some shale and sedimentary rocks (Ksh,t) are blue or reddish blue, but most sedimentary rocks and alluviums are green. The vegetation is depicted in black.

10-3. False color chemicals and ASTER meter band ratio depictions

For mapping metasediments and volcanoes, several band ratios of ASTER spectrometer images in the form of fake color composites (FCC) have been proposed. A color composition composed of the band ratios b5/b3 and b1/b2 expresses the spectral slope generated by the combined effect of iron absorption in the VNIR portion of the spectrum and the absence of Al-OH absorption in band 5. As RGB color pictures, false color combinations consisting of b4/b7, b3/b4, and b2/b1 are employed to distinguish volcanic rocks from sedimentary rocks (Abdeen et al. 2001). Band ratios b7/b6, b6/b5, and b6/b4 are utilized as RGB color

images to map gneiss domes and granites (Wolters et al., 2005), whereas band ratios b8/b5, b5/b4, and b7/b8 are used as RGB color images to detect alkaline granites (Madani and Emam 2009).

Vegetation is a significant source of error in satellite image lithology mapping. Vegetation can obfuscate the spectral features of a rock layer, preventing the identification of rock lithology. This is especially severe and problematic on the surfaces of some igneous rocks made of low-albedo materials (Grebby et al. 2014). In different periods of youth and senescence, vegetation can exhibit distinct spectral properties (Baldridge et al. 2009). Therefore, green and dry vegetation can react differently and simulate the spectral properties of various rocks and minerals (Grebby et al. 2014; Rasouli Beirami and Tangestani 2020). The Normalized Difference Vegetation Index (NDVI) is defined as (b3-b2)/(b3+b2) (Bertoldi et al. 2011; Meer et al. The lowest threshold in the NDVI image was chosen to cover the plant cover in the northwestern portion of the research area, where the vegetation cover is extremely dense.

The form of the rock spectra in the VNIR region of the spectrum is often impacted by the absorption intensity of ferric iron and iron (Rowan, Mars, and Simpson 2005). (Rowan, Mars, and Simpson 2005). Iron-ferric adsorption decreases band 1 reflectance. Fe has a greater b1/b2 ratio because its absorption in band 1 is not as intense.

(b7 + b9) / (b8 + b8) is sensitive to the adsorption of Fe-OH and Mg-OH in epidote, chlorite, and other ferromnesian minerals in the research area (Dalton et al. 2004; Rasouli Beirami and Tangestani 2020) Consequently, it is common knowledge that Fe-OH, Mg-OH, and CO3 absorption features cannot be separated based on relative band depth estimations alone ((Rowan and Mars 2003; Dalton et al. 2004)). In order to distinguish carbonate rocks from igneous rocks, albedo must also be considered. The albedo of carbonate rocks is typically greater than that of volcanic rocks and other types of igneous rocks ((Rasouli Birami and Tangestani 2020)).

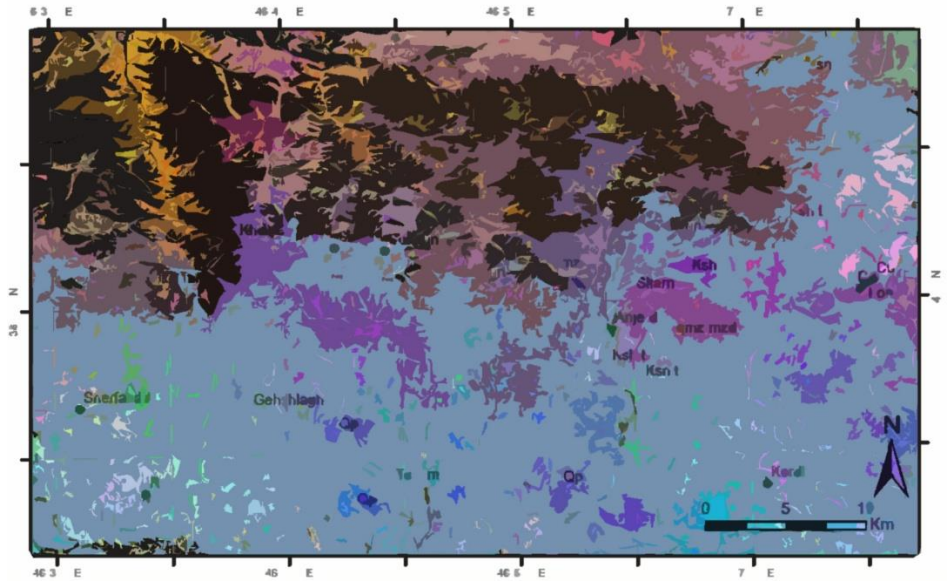

Fig. 5. False color combination (FCC) b4/b7, b3/b4, and b2/b1 are depicted in Figure 5. The majority of sedimentary rocks are light green in color, with the exception of shale (Ksh,t) and limestone, which are blue or reddish blue. Quartz monzonite (qmz-mzd) and monzonite (mz), as well as other intrusive and volcanic rocks, are blue, bluish-red, or red. The vegetation is depicted in black.

Figure 5 depicts a composite image using the band ratios b4/b7, b3/b4, and b2/b1 for an RGB color image. Zero-based digital numbers were allocated to vegetation in order to highlight the color diversity of the rock units in question. As illustrated, volcanic and igneous rocks are colored red, pink, or blue. Sedimentary lands, in comparison, appear greener in the image. The FCC and PCA images are comparable. This demonstrates that the PCA image reflects the alterations in spectral characteristics in this false color mixture. In the figure, volcanic and igneous rocks have high ratios of 7.4 and 1.2 and low b3/b4 ratios compared to sedimentary terranes, which have mostly high b3/b4 ratios. Consequently, sedimentary rocks can be separated from volcanic and igneous rocks by thresholding the b3/b4 band ratio. Figure 6 depicts the outcome of b3/b4 thresholding after overlaying the findings on the geological map depicted in Figure 6. As the figure demonstrates, in most regions Astana has been able to identify sedimentary rocks from igneous rocks. The region indicated by r01, r02, and r03. In the above-threshold regions, it indicates that the rocks must be sedimentary, yet the lithology map indicates that they are volcanic. In addition, the majority of tuff and volcanic rocks are classed as either igneous or volcanic rocks. The threshold indicates that the rocks in regions r04 and r05 are of volcanic and igneous origin, however the lithology map indicates that they are of sedimentary origin.

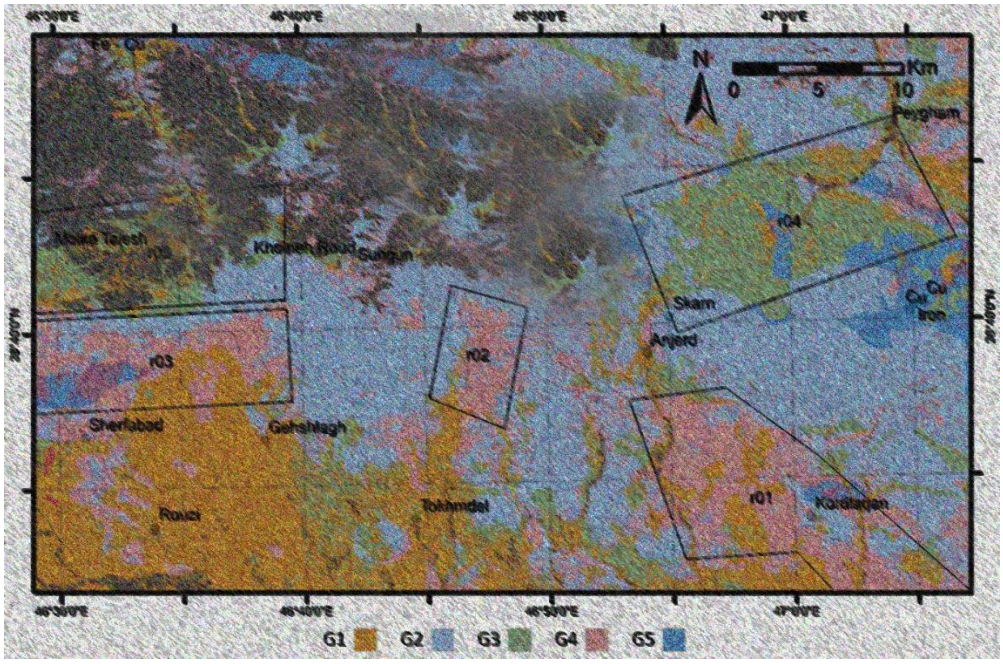

Fig. 6. depicts sedimentary rocks with a high b3/b4 band ratio, G2 volcanic and igneous rocks with a low b3/b4 band ratio, G3 sedimentary rocks with a low b3/b4 band ratio, G4 igneous or volcanic rocks with a high b3/b4 band ratio, and G5 tuff and volcanoclastic rocks with a predominantly low b3/b4 band ratio. In areas r01, r02, and r03, volcanic rocks have high b3/b4 band ratios, whereas sedimentary rocks have low b3/b4 band ratios in regions r04 and r05. The vegetation is depicted in black.

The change of ferromagnesian minerals into quartz, chlorite, epidote, calcite, dolomite, and albite is known as propylitic alteration (Sinclair 2007). Phyllic alteration zones, on the other hand, are made of quartz, sericite, and pyrite. In addition, argillic alteration is composed of quartz, illite, pyrite, kaolinite, smectite, montmorillonite, and calcite (Sinclair 2007). Except for quartz, which is infrared passive in the SWIR spectrum region, other propylitic alteration minerals absorb in band 8 of the ASTER spectrometer and partially in band 7 (Dalton et al. 2004; Rasouli Beirami and Tangestani 2020). Consequently, propylitic alteration can be identified with the ASTER meter's propylitic alteration mineral index (b6 b9)/(b8 b8). Due to the presence of Fe and Mg oxides, ferromagnesium minerals typically absorb in bands 7 and 8 (Singer 1981; Crown and Pieters 1987; Horgan et al. 2014) (Rowan and March 2003). Consequently, the preceding

index can also identify magnesium minerals. In the absence of mafic rocks, however, the aforementioned mineral index reveals propylitic alteration zones. Figure 7 depicts the propylitic alteration zones determined by the aforementioned procedure. It is evident that the propylitic alteration zone has damaged portions of the monzonitic mass of Shiwal Daghi.

Illite, kaolinite, sericite, and other clay minerals, which are more numerous in the mineralization of phyllic and argillic alteration zones, exhibit ASTER gauge band 6 absorption. Therefore, the presence of these minerals can be recognized with the Bierwith clay mineral index, which is (b5 b7)/(b6 b6) (Bierwith 2002; Kalinowski and Oliver 2004; Testa et al. 2018), or similarly with the (b5 b7)/(b6 b6) ratio (Bierwith 2002; Kalinowski and Oliver 2004; Testa et al Using the band ratio picture (b5+b7)/b6 (Rowan and Mars, 2003) or (b4 + b7) / (b6 + b6) (Rowan, Mars, and Simpson, 2005), objects are categorized. Additionally, these band ratios can be utilized to detect silt and clay in alluvial deposits (Rasouli Beirami and Tangestani 2020). This index can be used to delineate zones of argillic and phyllic alteration where the rocks are igneous or volcanic. The argillic alteration distribution zones obtained using the method described above indicate that the argillic alteration zones in granodiorite, monzonite, dacite, trachyte, and ignimbrite rocks are more widespread in the vicinity of the Songon copper deposit and up to approximately 8 kilometers south of the deposit. This supports the relationship between copper deposits and intense alteration halos (Hezarkhani 2006). Except in the region of the skarn rock unit in the northern portion of the intrusive mass, the Shiver Dagh quartz-monzonite intrusive mass shows no indications of argillic alteration.

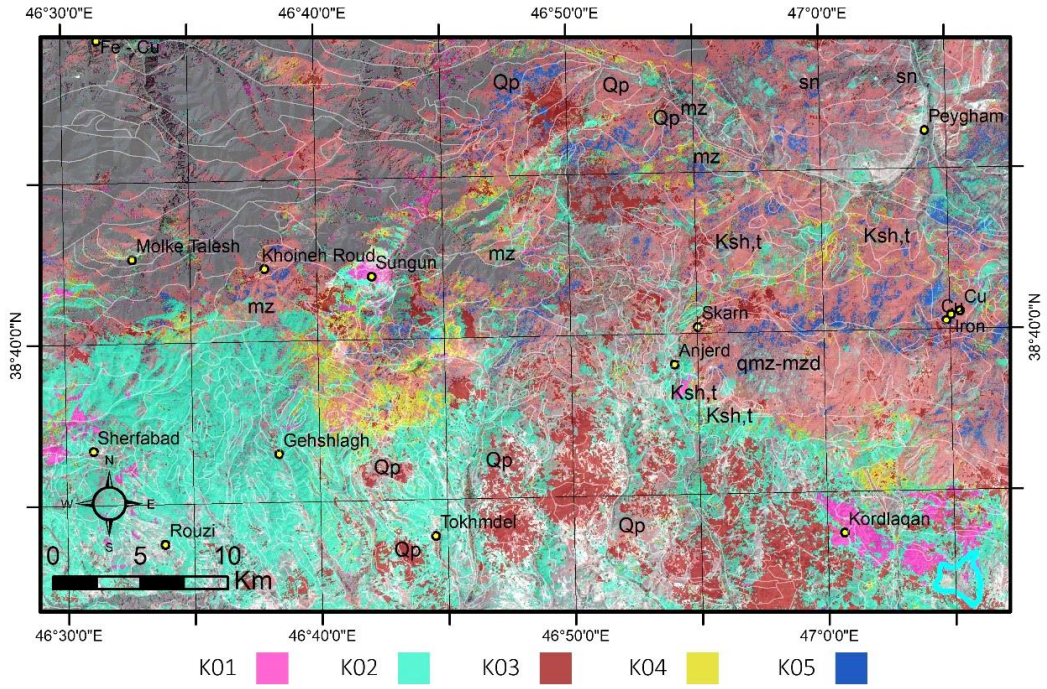

Fig. 7. A lithological map of the research area generated using MF, SAM, and band ratio estimates. K01 refers to extensively altered volcanic rocks, K02 to sedimentary rocks recognized by MF, and K03 to dark basalts with a larger concentration of ferromagnesian minerals, such as pyroxene. K04 and K05 display zones of argillic and propylitic alteration, respectively.

10-4. Images captured by the Spectral Angle Mapper (SAM)

Figure 3 depicts a variety of igneous rock units that were entered into the SAM algorithm to evaluate its rock mapping capabilities. The SAM algorithm could differentiate between igneous and volcanic rocks,

sedimentary rocks, and alluvial deposits. The outcome of the SAM method in differentiating sedimentary rocks from igneous and volcanic rocks was quite comparable to Figure 4's PCA image and Figure 5's b3/b4 band ratio image. Although the SAM algorithm is sufficiently sensitive to the spectral difference between volcanic and sedimentary rocks, the results indicate that it is not sensitive to the spectral alterations of lithological units that are more comparable. In addition, the generated SAM images have a low standard deviation of the digital values of the image pixels, making the distinction between the target and the backdrop confusing. The SAM algorithm was therefore not chosen for further image processing.

10-5. Matching Filtering (MF) photographs

Figure 3 depicts spectra that were entered into the matched filtering (MF) algorithm to evaluate its efficacy. Figure 7 demonstrates the outcomes. Figure 3 depicts the spectrum inputs chosen for the program. As depicted in Figure 2, the spectral distinction between igneous and volcanic rocks is quite slight, and the typical spectrometer images cannot distinguish between them. Similar to the SAM algorithm, the MF algorithm is incapable of distinguishing between volcanic and igneous rocks.

Real color composite pictures from Landsat 8 reveal altered ignimbrite and significantly altered volcanic rocks with the absorption properties of ferric iron oxides in the southernmost portion of the study area. These stones have low PCA band 5 pixel values. Figure 3 illustrates the spectrum of these stones. The average spectrum of the stone unit has been entered into the MF algorithm in order to identify these stones. Figure 7 demonstrates that the MF algorithm is capable of detecting these extensively changed rocks. The majority of Songun copper deposit rocks are also significantly changed and exhibit the distinctive absorption properties of ferric iron oxides. This is because ongoing mining in the deposit has caused extensive weathering and dissolution of sulfur minerals, as well as the release of iron from copper-iron sulfides such as pyrite. Figure 7 depicts rocks that have been significantly changed by K01 in the rectangular regions r07 and r08.

As depicted in Figure 7, MF is also capable of distinguishing dark basaltic rocks and igneous rocks with a larger proportion of pyroxene and/or olivine minerals (characterized by K03) from other igneous rocks.
Clay and shale minerals share ASTER gauge band 6 absorption properties. To recognize clay-rich sedimentary rocks such as shale, the MF algorithm was fed the spectrum of argillaceous sedimentary rocks recovered from the IARR image as shown in Figure 3. The results indicate that the majority of sedimentary clastic rocks in the region are intermixed with volcanic clastic elements, and that the extent of pure sedimentary rocks is extremely limited. In reality, a comprehensive investigation of the region's geological maps reveals that the sedimentary rocks of the region under study contain a considerable amount of volcanic components. Most volcanic rocks have reached the alluvial cone, particularly in the southern portion of the investigated region. In these regions, sedimentary and volcanic rocks are therefore intricately intermixed and cannot be separated using the MF method.

The areas with the largest abundance of argillic materials were separated using the band ratio (b5 b7) / (b6 b6) and the resulting image was overlaid with volcanic and magmatic rocks to detect argillic alteration. Similarly, the band ratio (b6 b9) / (b8 b8) was covered by igneous and volcanic rocks to reveal propylitic alteration. Figure 7 depicts the results respectively.

11. CONCLUSION

By studying satellite photos, it was discovered that the spectral features of igneous and volcanic rocks in the area of study are nearly identical. This is due to the poor SWIR spectrum characteristics of quartz and feldspar. However, it has been demonstrated that a combination of PCA, MF, and band ratio may be used to distinguish igneous and volcanic rocks from sedimentary rocks and to identify argillic and propylitic alteration zones. Around the Songun porphyry copper deposit, the most significant argillic alteration and

moderate propylitic alteration were seen. Except for the region of the skarn deposit, there is no argillic alteration in the Shiver Daghi monzonitic bulk. In contrast, substantial propylitic alteration occurs in the monzonite mass of Shiver Daghi. It is determined that the value of ASTER images for mapping areas containing igneous and volcanic rock units is restricted, but mapping such areas with the proper techniques can provide important information and likely disclose the locations of porphyry copper mineralization.

REFERENCES

Abdeen, M.M., Allison, T.K., Abdelsalam, M.G., & Stern, R.J. (2001). Application of ASTER band-ratio images for geological mapping in arid regions; the Neoproterozoic Allaqi Suture, Egypt. Abstract with Program Geological Society of America, 3(3), 289.

Adams, J.B., Goullaud, L.H. (1978). Plagioclase feldspars-Visible and near infrared diffuse reflectance spectra as applied to remote sensing. In In: Lunar and Planetary Science Conference, 9th, Houston, Tex., March 13-17, 1978, Proceedings. Volume 3.(A79-39253 16-91) New York, Pergamon Press, Inc., 1978, p. 2901-2909. (Vol. 9, pp. 2901-2909).

Agard, P., Omrani, J., Jolivet, L., Whitechurch, H., Vrielynck, B., Spakman, W., Wortel, R. (2011). Zagros orogeny: a subduction-dominated process. Geological Magazine, 148(5-6), 692-725.

Ashrafi, N., Pourmohsen, M., Faridazad, M. (2023) Study of A-type granite from the South of Lake Urmia, Sanandaj-Sirjan Zone: implications for the Neotethys opening in Iran, Iranian Journal of Earth Sciences 15 (2): 121-139

Bazoobandi, M.H., Arian, M.A., Emami, M.H., Tajbakhsh, G.R., Yazdi, A. (2015) Geodynamics of Dikes in North of Saveh, Open Journal of Ecology 5(09): 452-459

Baldridge, A.M., Hook, S.J., Grove, C.I., Rivera, G. (2009). The ASTER spectral library version 2.0. Remote sensing of environment, 113(4), 711-715.

Ben-Dor, E., Kruse, F.A. (1994). The relationship between the size of spatial subsets of GER 63 channel scanner data and the quality of the Internal Average Relative Reflectance (IARR) atmospheric correction technique. Remote Sensing, 15(3), 683-690.

Bertoldi, L., Massironi, M., Visonà, D., Carosi, R., Montomoli, C., Gubert, F., Pelizzo, M.G. (2011). Mapping the Buraburi granite in the Himalaya of Western Nepal: remote sensing analysis in a collisional belt with vegetation cover and extreme variation of topography. Remote Sensing of Environment, 115(5), 1129-1144.

Bierwith, P. (2002). Evaluation of ASTER satellite data for geological applications: Consultancy report to Geoscience Australia (Unpublished).

Bina, M., Arian, M.A., Pourkermani, M., Bazoobandi, M.H., Yazdi, A. (2020) Study of the petrography and tectonic settings of sills In Lavasanat district, Tehran (north of Iran), Nexo Revista Cientifica, 33(2), 286-296.

Boardman, J.W., Kruse, F. A., Green, R.O. (1995, January). Mapping target signatures via partial unmixing of AVIRIS data. In Summaries of the Fifth Annual JPL Airborne Earth Science Workshop. Volume 1: AVIRIS Workshop.

Crosta, A.P. (1989). Enhancement of Landsat Thematic Mapper imagery for residual soil mapping in SW Minas Gerais State Brazil, a prospecting case history in greenstone belt terrain. In Proceedings of the 7^< th> ERIM Thematic Conference on Remote Sensing for Exploration Geology, 1989.

Crowley, J.K. (1993). Mapping playa evaporite minerals with AVIRIS data: A first report from Death Valley, California. Remote Sensing of Environment, 44(2-3), 337-356.

Crowley, J.K., Brickey, D.W., Rowan, L.C. (1989). Airborne imaging spectrometer data of the Ruby Mountains, Montana: mineral discrimination using relative absorption band-depth images. Remote Sensing of Environment, 29(2), 121-134.

Crown, D.A., Pieters, C.M. (1987). Spectral properties of plagioclase and pyroxene mixtures and the interpretation of lunar soil spectra. Icarus, 72(3), 492-506.

Dalton, J.B., Bove, D.J., Mladinich, C.S., Rockwell, B.W. (2004). Identification of spectrally similar materials using the USGS Tetracorder algorithm: the calcite–epidote–chlorite problem. Remote Sensing of Environment, 89(4), 455-466.

Gao, B.C., Montes, M.J., Davis, C.O., & Goetz, A.F. (2009). Atmospheric correction algorithms for hyperspectral remote sensing data of land and ocean. Remote sensing of environment, 113, S17-S24.

Gharib-Gorgani, F., Ashja-Ardalan, A., Espahbod, M.R., Sheikhzakariaee, S.J., Yazdi, A. (2017) Petrology of Mg-bearing Meta Ophiolite Complexes of Qaen-Gazik, Eastern Iran, National Cave Research and Protection Organization 4(1), DOI:10.21276/ambi.2017.04.1.ga01

Grebby, S., Cunningham, D., Tansey, K., Naden, J. (2014). The impact of vegetation on lithological mapping using airborne multispectral data: A case study for the north Troodos region, Cyprus. Remote Sensing, 6(11), 10860-10887.

Hezarkhani, A. (2006). Petrology of the intrusive rocks within the Sungun porphyry copper deposit, Azerbaijan, Iran. Journal of Asian Earth Sciences, 27(3), 326-340.

Horgan, B.H., Cloutis, E.A., Mann, P., Bell III, J.F. (2014). Near-infrared spectra of ferrous mineral mixtures and methods for their identification in planetary surface spectra. Icarus, 234, 132-154.

Hunt, G.R. (1977). Spectral signatures of particulate minerals in the visible and near infrared. Geophysics, 42(3), 501-513.

Hunt, G.R., Salisbury, J.W Lenhoff. C.R. (1972). Visible and nearinfrared spectra of minerals and rocks: V. Halides, phosphates, arsenates, vanadates, and borates." Modern Geology 3:121– 32.

Jalali Nezhad, T., Masoumi, H.R., Dehghanian, M.S., Tarrah, J, (2023) Geochemistry and potential of toxic elements in sediments originating from salt domes, north of Hormuz strait (Pol, Gachin, Angouran and Hormuz), Iranian Journal of Earth Sciences 15 (1): 54-65

Kalinowski, A., Oliver, S. (2004). ASTER mineral index processing manual. Remote Sensing Applications, Geoscience Australia, 37, 36.

Kruse, F.A., Lefkoff, A.B., Boardman, J.W., Heidebrecht, K.B., Shapiro, A.T., Barloon, P.J., Goetz, A.F.H. (1993). The spectral image processing system (SIPS)—interactive visualization and analysis of imaging spectrometer data. Remote sensing of environment, 44(2-3), 145-163.

Kruse, F.A. (1988). Use of airborne imaging spectrometer data to map minerals associated with hydrothermally altered rocks in the northern grapevine mountains, Nevada, and California. Remote Sensing of Environment, 24(1), 31-51.

Madani, A.A., Emam, A.A. (2009). SWIR ASTER band ratios for lithological mapping and mineral exploration: a case study from El Hudi area, southeastern desert, Egypt. Arabian journal of Geosciences, 4(1), 45-52.

Moghadam, A.R., Lotfi, M., Jafari, M.R., Ardalan, A.A., Moghaddam, M.P., Yazdi, A. (2021) Economic Geology, Petrology and Environmental of Copper Ore Deposits of Chagho in South West Karaj, Revista Geoaraguaia 11(1): 7-26

Moinevaziri, H., Azizi, H. (2023) Is skarnization the cause of mineralization? a case study, Sanandaj Sirjan zone, west Iran, Iranian Journal of Earth Sciences 15 (1): 1-9

Naeemi, S., Arian, M.A., Kohansal-Ghadimvand, N., Yazdi, A., Abedzadeh, H. (2022) Diagenesis and Tectonic Setting of the Varcheh Intrusive Masses in Sanandaj-Sirjan Zone, Iran, Revista Geoaraguaia 12 (1): 52-72

Pirmohammadi Alishah, F. (2023) Genesis and geochemical evolution of the Mio-Pliocene volcanic rocks in the SW of Bostanabad, NW Iran: A comparison with the classic Adakite, Iranian Journal of Earth Sciences 15 (2): 106-120

Rahimzadeh, B., Ghosoun, Z.H., Masoudi, F. (2022) Identification of Fe3+ content in Epidote from Varan, Urumieh-Dokhtar magmatic arc, Iran: using FTIR and Raman spectroscopy, Iranian Journal of Earth Sciences 14 (2): 131-139

Rajendran, S., Hersi, O.S., Al-Harthy, A., Al-Wardi, M., El-Ghali, M.A., Al-Abri, A.H. (2011). Capability of advanced spaceborne thermal emission and reflection radiometer (ASTER) on discrimination of carbonates and associated rocks and mineral identification of eastern mountain region (Saih Hatat window) of Sultanate of Oman. Carbonates and Evaporites, 26, 351-364.

Rajendran, S., Nasir, S., Kusky, T.M., Ghulam, A., Gabr, S., El-Ghali, M.A. (2013). Detection of hydrothermal mineralized zones associated with listwaenites in Central Oman using ASTER data. Ore geology reviews, 53, 470-488.

Rasouli Beirami, M., & Tangestani, M. H. (2020). A new band ratio approach for discriminating calcite and dolomite by ASTER imagery in arid and semiarid regions. Natural Resources Research, 29, 2949-2965.

Richter, R., & Schläpfer, D. (2013). Atmospheric/topographic correction for satellite imagery (ATCOR-2/3 User Guide, Version 8.3. 1, February 2014). ReSe Applications Schläpfer, Langeggweg, 3.

Rockwell, B. W., & Hofstra, A. H. (2008). Identification of quartz and carbonate minerals across northern Nevada using ASTER thermal infrared emissivity data—Implications for geologic mapping and mineral resource investigations in well-studied and frontier areas. Geosphere, 4(1), 218-246.

Rowan, L. C., & Mars, J. C. (2003). Lithologic mapping in the Mountain Pass, California area using advanced spaceborne thermal emission and reflection radiometer (ASTER) data. Remote sensing of Environment, 84(3), 350-366.

Rowan, L. C., Mars, J. C., & Simpson, C. J. (2005). Lithologic mapping of the Mordor, NT, Australia ultramafic complex by using the Advanced Spaceborne Thermal Emission and Reflection Radiometer (ASTER). Remote sensing of Environment, 99(1-2), 105-126.

RSI. 2004. "ENVI user's guide, the environment for visualizing images, version 4.1." In. Boulder, Colorado: Research Systems Incorporated.

Safari, M., Haji Babaei, A., Daya, A., Manouchehriniya, M. (2022) Separating geochemical anomalies by concentration- area, concentration-perimeter and concentration-number fractal models in Qaen region, East of Iran, Iranian Journal of Earth Sciences 14 (4): 271-284

Seyyedi, M., Lotfi, M., Gourabjeripour, A., Ashja Ardalan, A. (2022) Investigation of alterations and lineaments in Rashid-Abad mineral area (N Zanjan, NW Iran), Using integration of Remote Sensing and Aeromagnetic data, Iranian Journal of Earth Sciences 14 (4): 301-321

Sinclair, W. D. (2007). Porphyry deposits. Mineral deposits of Canada: A synthesis of major deposit-types, district metallogeny, the evolution of geological provinces, and exploration methods: Geological Association of Canada, Mineral Deposits Division, Special Publication, 5, 223-243.

Singer, R. B. (1981). Near-infrared spectral reflectance of mineral mixtures: Systematic combinations of pyroxenes, olivine, and iron oxides. Journal of Geophysical Research: Solid Earth, 86(B9), 7967-7982.

Tangestani, M. H., Mazhari, N., Agar, B., & Moore, F. (2008). Evaluating Advanced Spaceborne Thermal Emission and Reflection Radiometer (ASTER) data for alteration zone enhancement in a semi-arid area, northern Shahr-e-Babak, SE Iran. International Journal of Remote Sensing, 29(10), 2833-2850.

Testa, F. J., Villanueva, C., Cooke, D. R., & Zhang, L. (2018). Lithological and hydrothermal alteration mapping of epithermal, porphyry and tourmaline breccia districts in the Argentine Andes using ASTER imagery. Remote Sensing, 10(2), 203.

Wolters, J. M., Goldin, L., Watts, D. R., & Harris, N. B. W. (2005). Remote sensing of gneiss and granite in southern Tibet. Geol. Soci. America, Abstract with Program, 37, 5.

Yazdi, A., Ashja-Ardalan, A., Emami, M.H., Dabiri, R., Foudazi, M. (2019) Magmatic interactions as recorded in plagioclase phenocrysts of quaternary volcanics in SE Bam (SE Iran), Iranian Journal of Earth Sciences, 11(3): 215-224.

Yazdi, A., ShahHoseini, E., Razavi, R. (2016) AMS, A method for determining magma flow in Dykes (Case study: Andesite Dyke). Research Journal of Applied Sciences, 11(3), 62-67

Yazdi, A., Shahhosseini, E., Moharami, F. (2022) Petrology and tectono-magmatic environment of the volcanic rocks of West Torud–Iran, Iranian Journal of Earth Sciences 14 (1): 40-57

Yamaguchi, Y., & Naito, C. (2003). Spectral indices for lithologic discrimination and mapping by using the ASTER SWIR bands. International Journal of Remote Sensing, 24(22), 4311-4323.

Zaini, N., Van der Meer, F., & Van der Werff, H. (2014). Determination of carbonate rock chemistry using laboratory-based hyperspectral imagery. Remote sensing, 6(5), 4149-4172.